Supplementary Information

Securing cation vacancies to enable reversible Mg insertion/extraction in rocksalt oxides

Tomoya Kawaguchi,[1,*] Masaya Yasuda,[1] Natsumi Nemoto,[1] Kohei Shimokawa,[1,2] Hongyi Li,[1] Norihiko L. Okamoto,[1] and Tetsu Ichitsubo[1,†]

[1]*Institute for Materials Research, Tohoku University, Sendai, 9808577, Japan*

[2]*Frontier Research Institute for Interdisciplinary Sciences, Tohoku University, Sendai, 9808578, Japan*

[*]*tkawaguchi@imr.tohoku.ac.jp*, [†]*tichi@imr.tohoku.ac.jp*

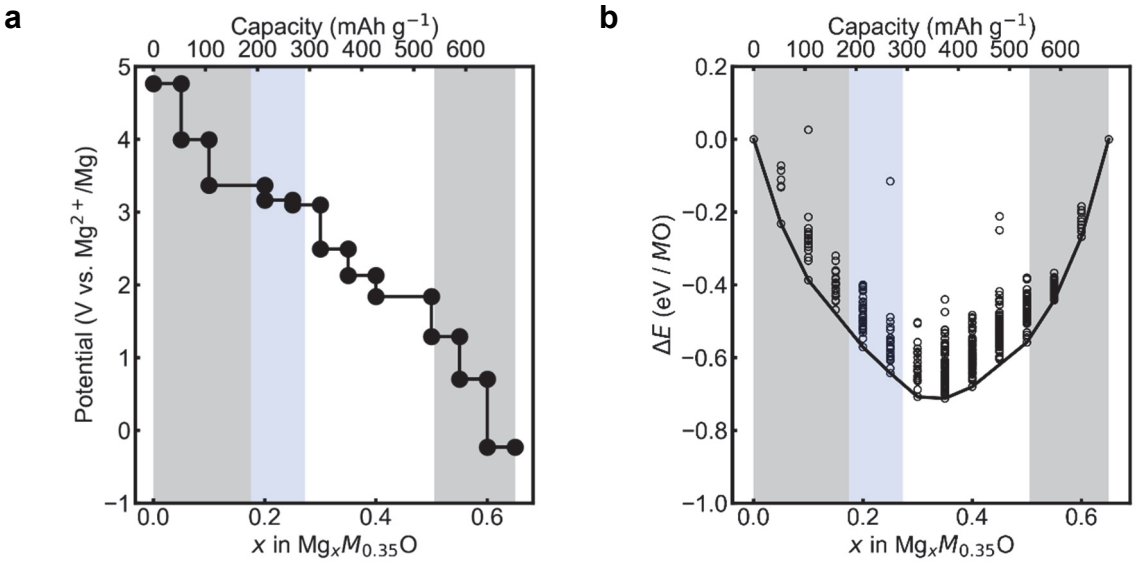

Figure S1. Electrode potential predicted by *ab initio* calculation. (a) Potential change as a function of Mg composition. (b) Formation energy of disordered rocksalt relative to the two-phase separation of $M_{0.35}Vac_{0.65}O$ and $Mg_{0.65}M_{0.35}O$. In (a) and (b), the Mg composition region from 0.275 to 0.5 with a white background represents the potentially available by the conventional redox of the constituent transition metals shown in Fig. 1b. The blue-colored region is extended available composition when Cr can be oxidized up to 6+. The gray-colored regions are prohibited compositions in light of the known valence state of the constituent transition metals and divalent oxygen.

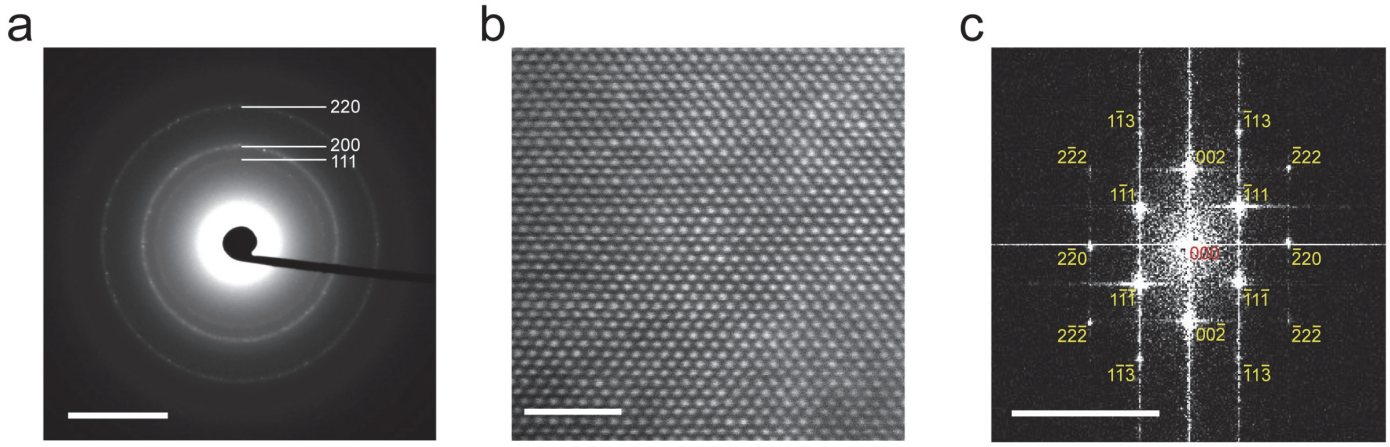

Figure S2. (a) Selected-area electron diffraction (SAED) of the M7O particles. (b)HAADF-STEM image along the [110] direction of a typical particle. (c) Fourier transform from the atomic images of (b). The scale bars in (a), (b), and (c) are 5 nm^{-1}, 2 nm and 10 nm^{-1}, respectively. All the Debye rings observed in SAED of (a) and bright spots (Bragg diffraction) in (c) can be indexed by the FCC symmetry, indicating that M7O forms the rocksalt structure.

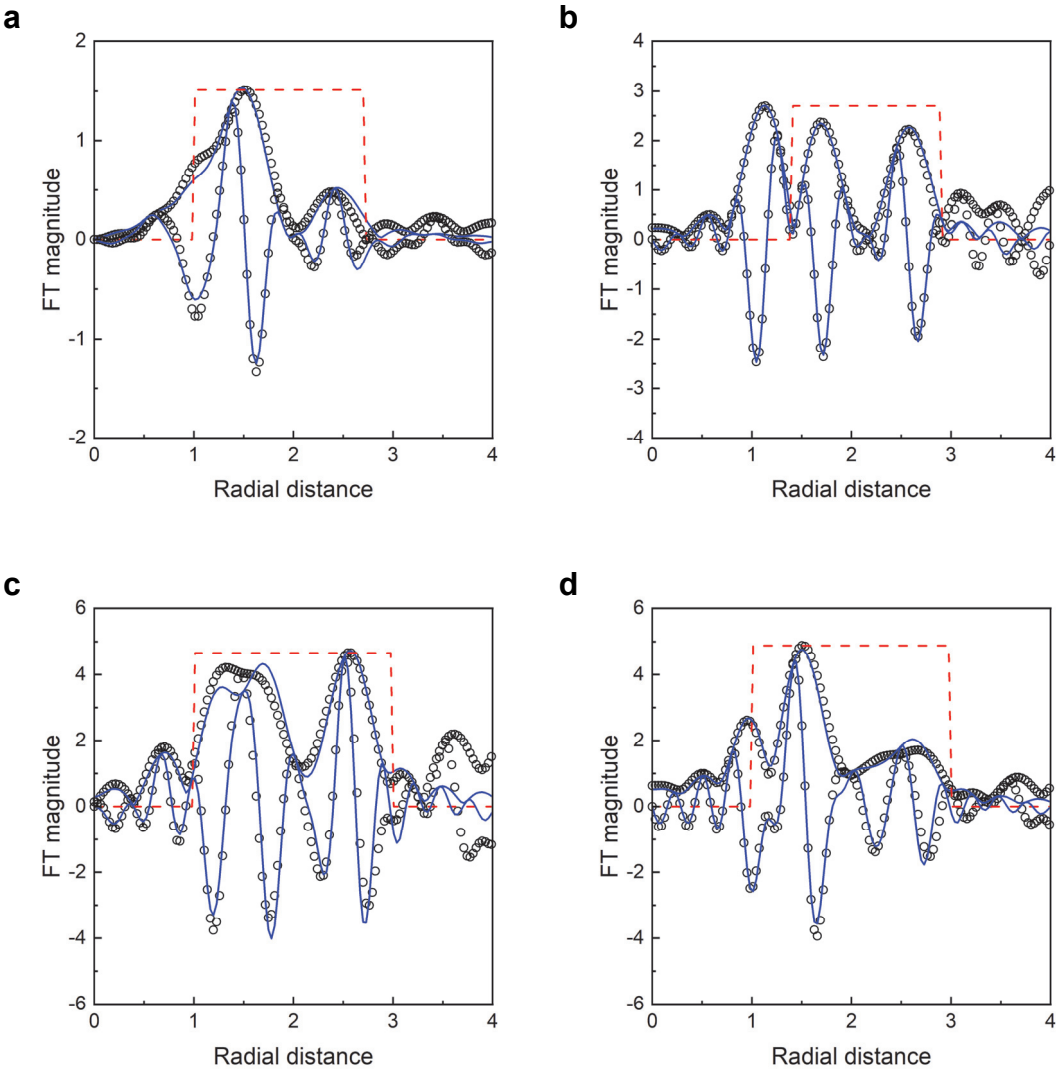

Figure S3. k^2-weighted FT amplitudes and imaginary parts from extended X-ray absorption fine structure of the as-synthesized M7O. (a) Cr, (b) Mn, (c) Fe, (d) Zn. Symbols and solid lines are for experimental data and least-squares fitting curves. Dashed lines delimit the fitting ranges used. Shown radial distances were underestimated because of the phase change of photoelectron wave by atomic potentials.

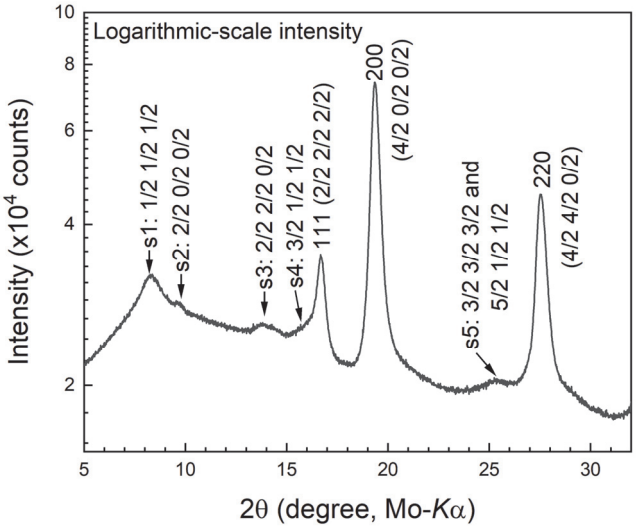

Figure S4. X-ray powder diffraction profiles of as-synthesized $Mg_{0.35}Li_{0.3}Cr_{0.1}Mn_{0.05}Fe_{0.05}Zn_{0.05}Mo_{0.1}O$ (M7O). The intensity was plotted on a logarithmic scale to clarify relatively weak peaks. Integer diffraction indexes (111, 200, and 220) represent fundamental X-ray diffraction (XRD) peaks that can be assigned by a basic cubic rocksalt structure. Weak peaks assigned by fractional diffraction indexes with notations of s1-s5 were attributed to a 2×2×2 superlattice of the basic cubic unit cell, implying the existence of a weak middle-range order of cations.

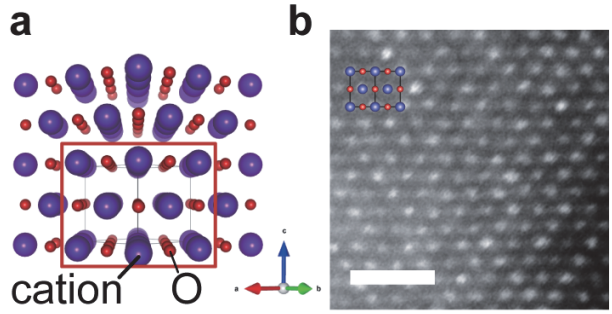

Figure S5. Scanning transmission electron microscopy (STEM) of the as-synthesized M7O particle with a diameter of < 10 nm. (a) Perspective view of cubic rocksalt oxide of M7O along [110] direction. (b) HAADF-STEM image along [110] of a small particle whose diameter was estimated to be less than 10 nm. In (b), a superimposed atomic illustration shows the positions of atomic columns. In the small particle of (b), a tone difference was observed at each cation column in contrast to the large particle shown in Fig. 1e. Since the heavier elements look brighter in the HAADF-STEM image, this tone difference hinted that there was somewhat fluctuation in the occupation state of light and heavy elements, which would be related to the middle-range order observed in the XRPD (Figure S4). This tone fluctuation at each cation column was hardly observed in the larger particle (Fig. 1e), presumably because such a fluctuation at each cation column was canceled by averaging more atoms along [110] direction in the larger particle. The scale bar in b is 1 nm.

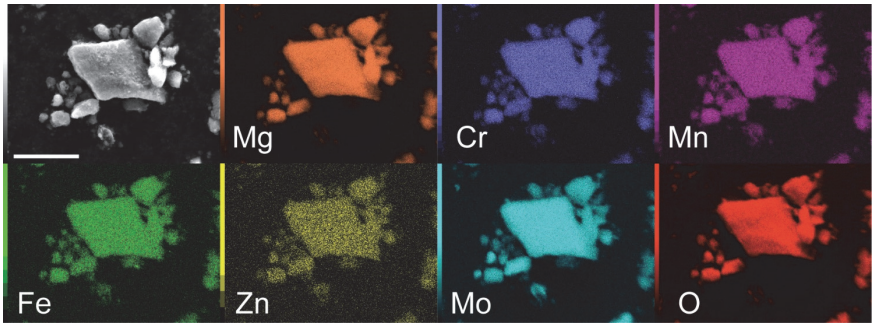

Figure S6. Scanning electron microscopy and energy dispersive spectroscopy (EDS) images of aggregated secondary particles of the as-synthesized M7O. The scale bar is 10 μm.

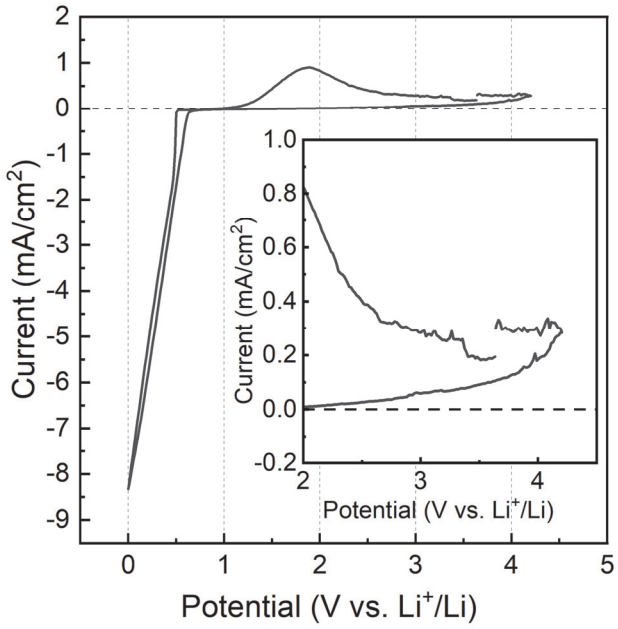

Figure S7. Cyclic voltammogram of the Mg deposition and stripping on a glassy carbon working electrode between 0 and 4.2 V vs. Li^+/Li with a scanning speed of 5 mV s^{-1} in the electrolyte of $Mg(TFSA)_2$/G3 with a 1:2 mol ratio at 90 °C. The cell configuration was the same as the ones used to evaluate the M7O active material except that the working electrode was the glassy carbon in the present measurement; the reference electrode (RE) was Li foil immersed in 0.5 M LiTFSA/DEME-TFSA electrolyte separated from the main bath by a ceramic filter, and the counter electrode (CE) was a Mg ribbon. The cathodic current below 0.7 V and anodic current around 1.8 V were attributed to the Mg deposition and stripping, respectively.

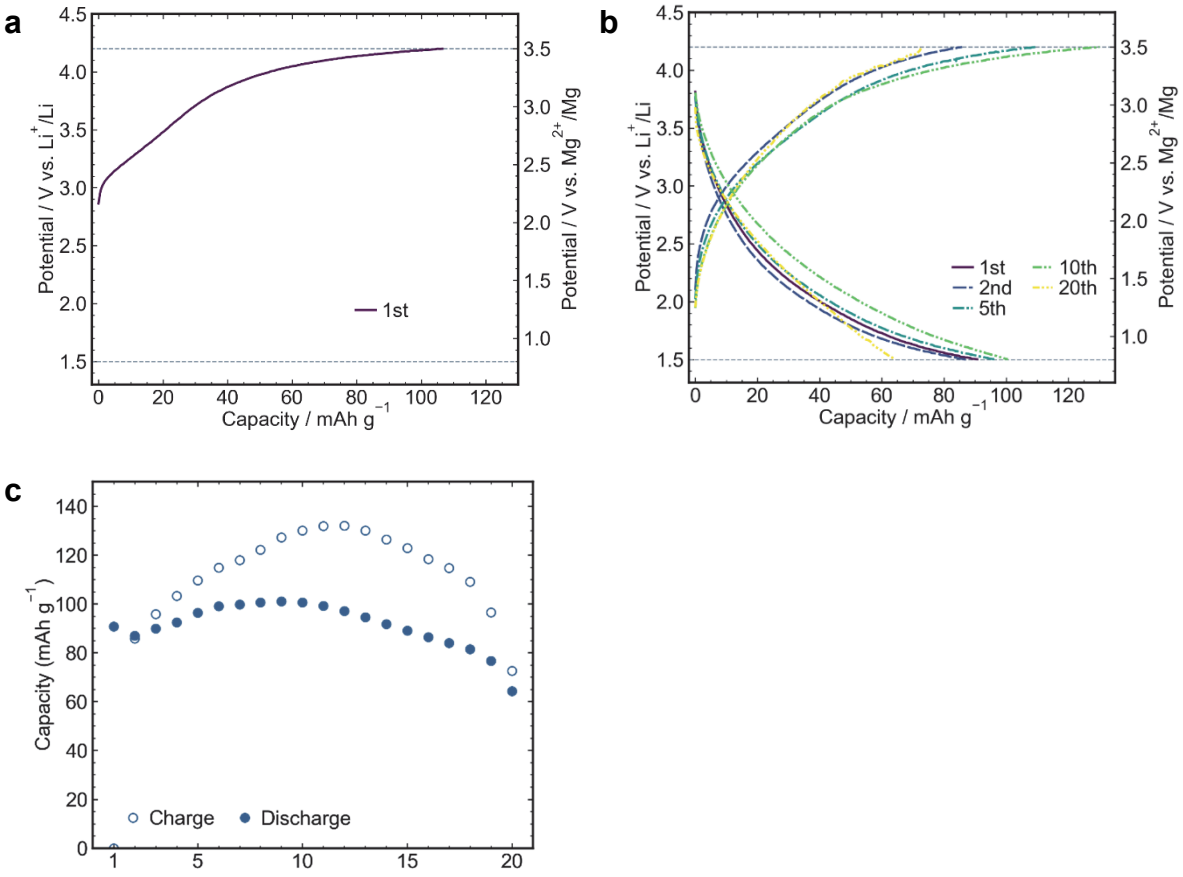

Figure S8. Charge discharge test with electrolyte replacement after the 1st charging. (a) Potential profile of M7O in the 1st charging. (b) Charge and discharge profiles after washing the charged electrode prepared in (a) followed by replacing the counter electrode and the electrolyte with virgin ones that did not contain Li cations. The cycle test started with discharging. (c) Capacity retention of (b). All tests were conducted at 90 °C with a current density of 10.4 mA g^{-1} within the potential window of 4.2 and 1.5 V for charging and discharging, respectively. This experiment indicates that the observed capacities after the 1st charge were predominantly attributed to Mg insertion/extraction rather than Li because Li cations extracted from the material in the 1st charge were eliminated both from the electrode and electrolyte.

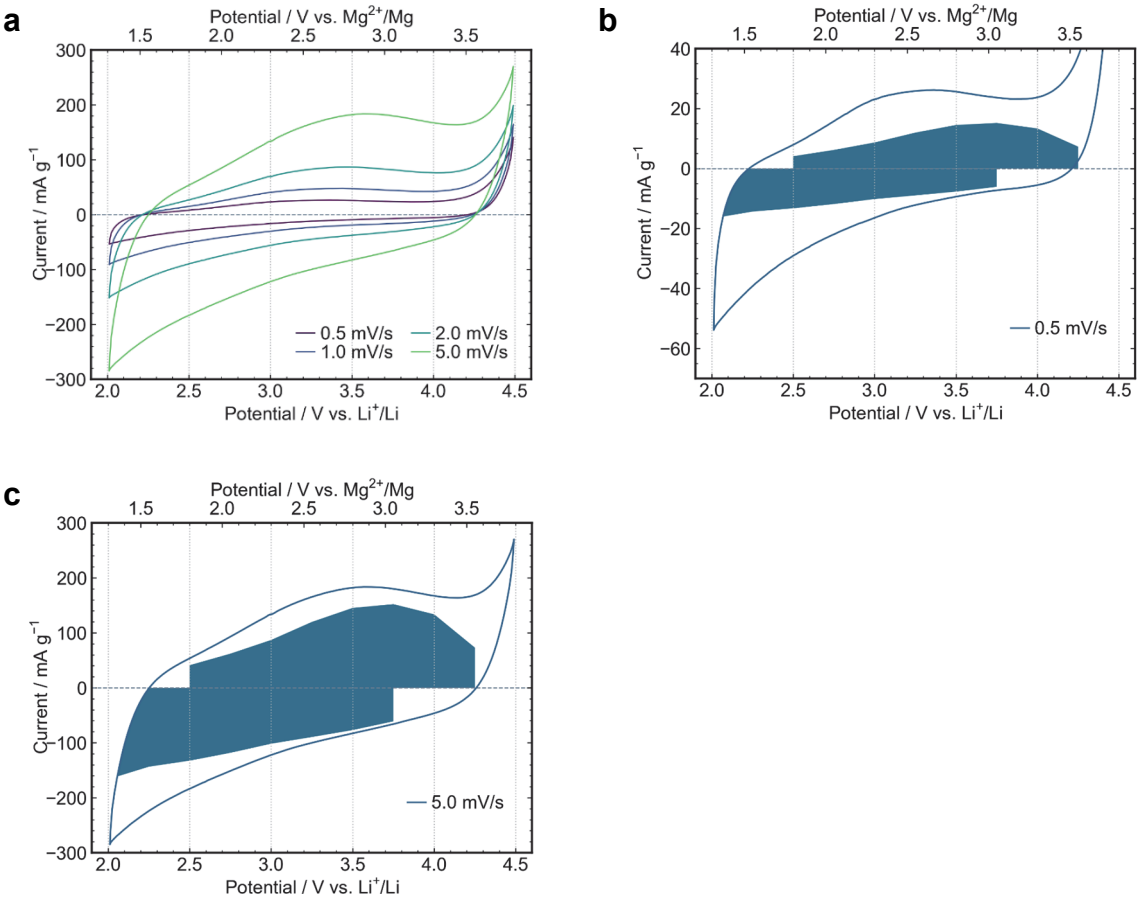

Figure S9. Electrochemical capacitive contribution analysis by cyclic voltammetry. (a) Cyclic voltammograms of the M7O cathode material between 2.0 and 4.5 V vs. Li^+/Li with different scanning speeds from 0.5 to 5 mV s^{-1} at 90 °C. (b-c) The cyclic voltammogram at (b) 0.5 and (c) 5 mV s^{-1}, in which the current contribution from electrochemical capacitor reaction was shown as the navy-colored area, determined by a two-speed kinetics model of the electrochemical reactions.[1–3] The analyses were carried out from 2.5 to 4.25 V vs. Li RE for anodic current and 2.05 to 3.25 for cathodic current. The slower scan rate of 0.5 mV s^{-1} in (b) showed that the CV current was predominantly from the intercalation contribution (i.e., less capacitive contribution) in contrast to CV with the faster scan rate of 5 mV s^{-1} in (e). Nevertheless, the scan rate of 0.5 mV s^{-1}, which was the slowest CV scan rate ever performed in the present study, was still much faster than the time scale of the typical charge/discharge tests. The former took 2.8 hours for a single cycle, while the latter typically took 20 hours. The intercalation contributions to the measured capacities were therefore expected to be more predominant in the charge/discharge tests.

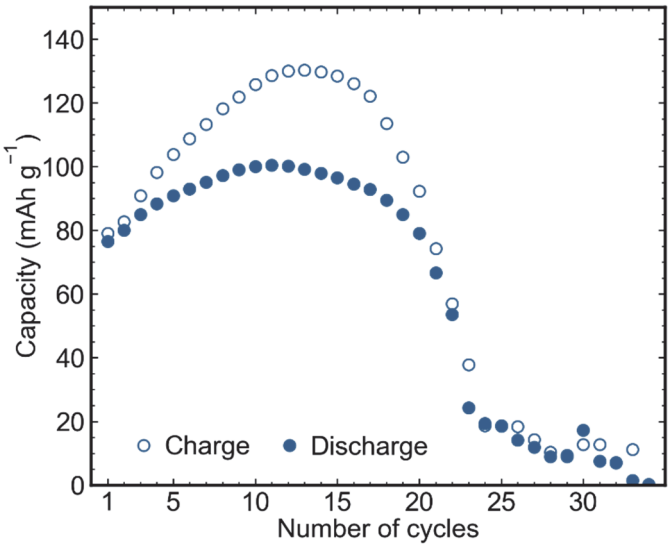

Figure S10. Extended capacity retention of the charge/discharge test. The tests were conducted at 90 °C with a current density of 10.4 mA g^{-1} within the potential window of 4.2 and 1.5 V for charging and discharging, respectively.

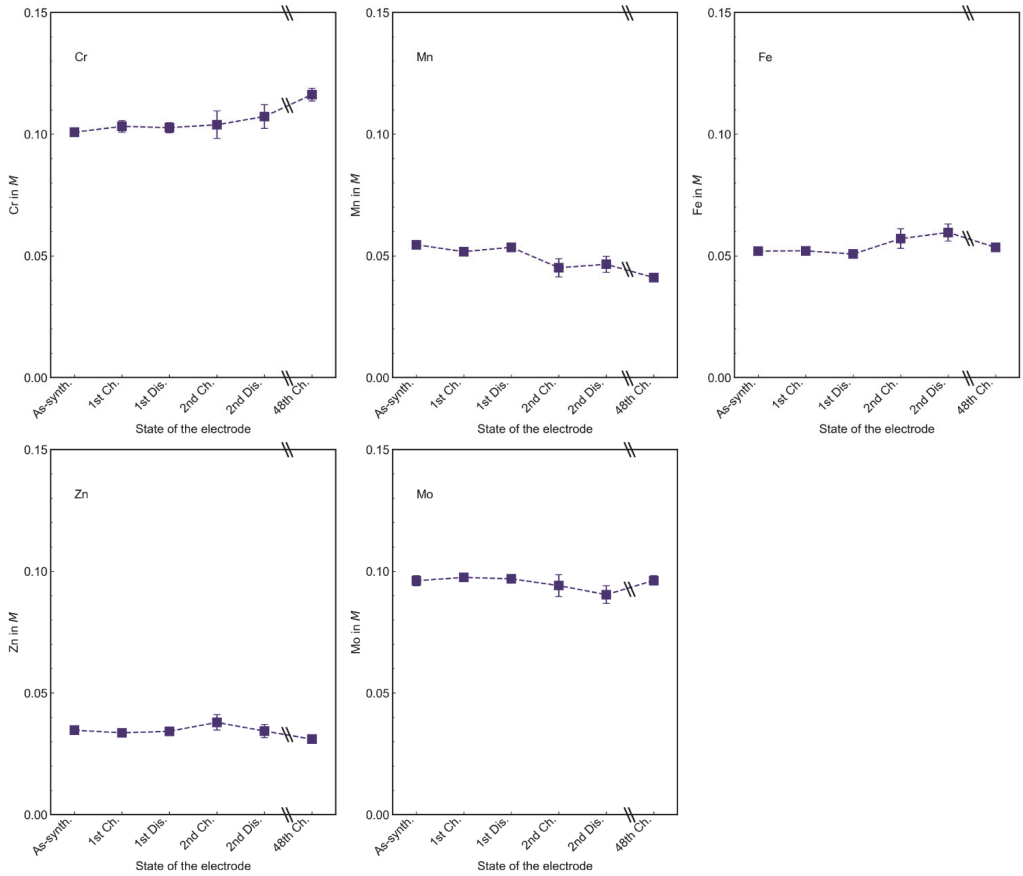

Figure S11. Compositions of the transition metals with increasing cycles determined by ICP-OES. Scale break lines (\\) indicate a large gap in the cycle number.

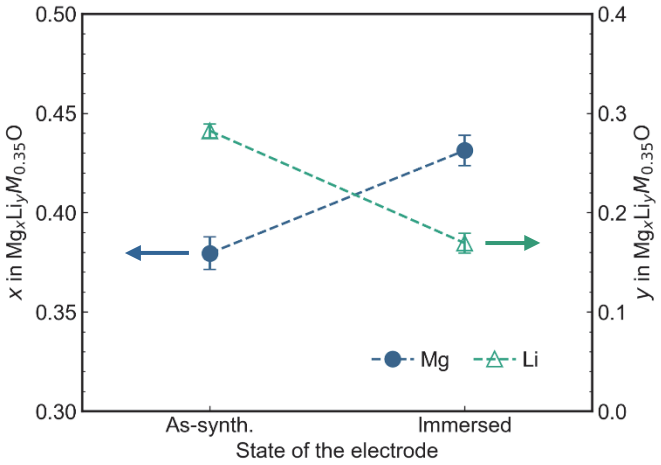

Figure S12. Spontaneous ion exchange between Mg and Li in M7O immersed in the electrolyte. A pristine electrode was immersed in an electrolyte of $Mg(TFSA)_2$/triglyme = 1/2 in mol ratio at 90 °C for 16 h without connecting any outer circuit. This indicates that both Mg^{2+} and Li^{+} were mobile in the material at 90 °C, and their ion exchange spontaneously occurred without current flow in the outer circuit. Half of the increased Mg composition was in excellent agreement with the decreased Li composition, which indicates that the total valence of the material was preserved in the ion exchange process.

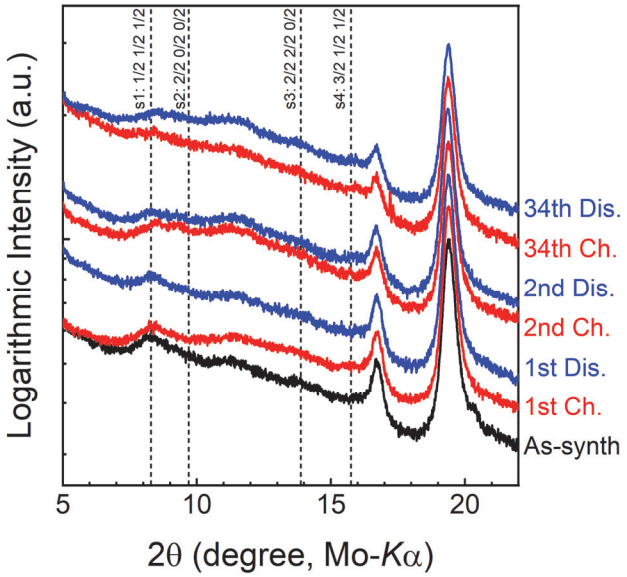

Figure S13. X-ray diffraction profiles of the charged/discharged M7O electrodes at low angle region in logarithmic scale. The intensity was plotted on a logarithmic scale to clarify relatively weak peaks. Vertical broken lines with fractional diffraction indexes and notations of s1-s4 represent the scattering angles where the superlattice peaks were observed in the as-synthesized M7O powder in Figure S4. The XRD profiles were acquired from the composite electrode by the Debye-Scherrer geometry. The profiles were, therefore, overlapped with the other components of the electrodes, such as carbon black and binder, as well as the glass capillary, in contrast to the XRD profile shown in Figure S4, where XRD of the pure active material was measured in Bragg-Brentano geometry.

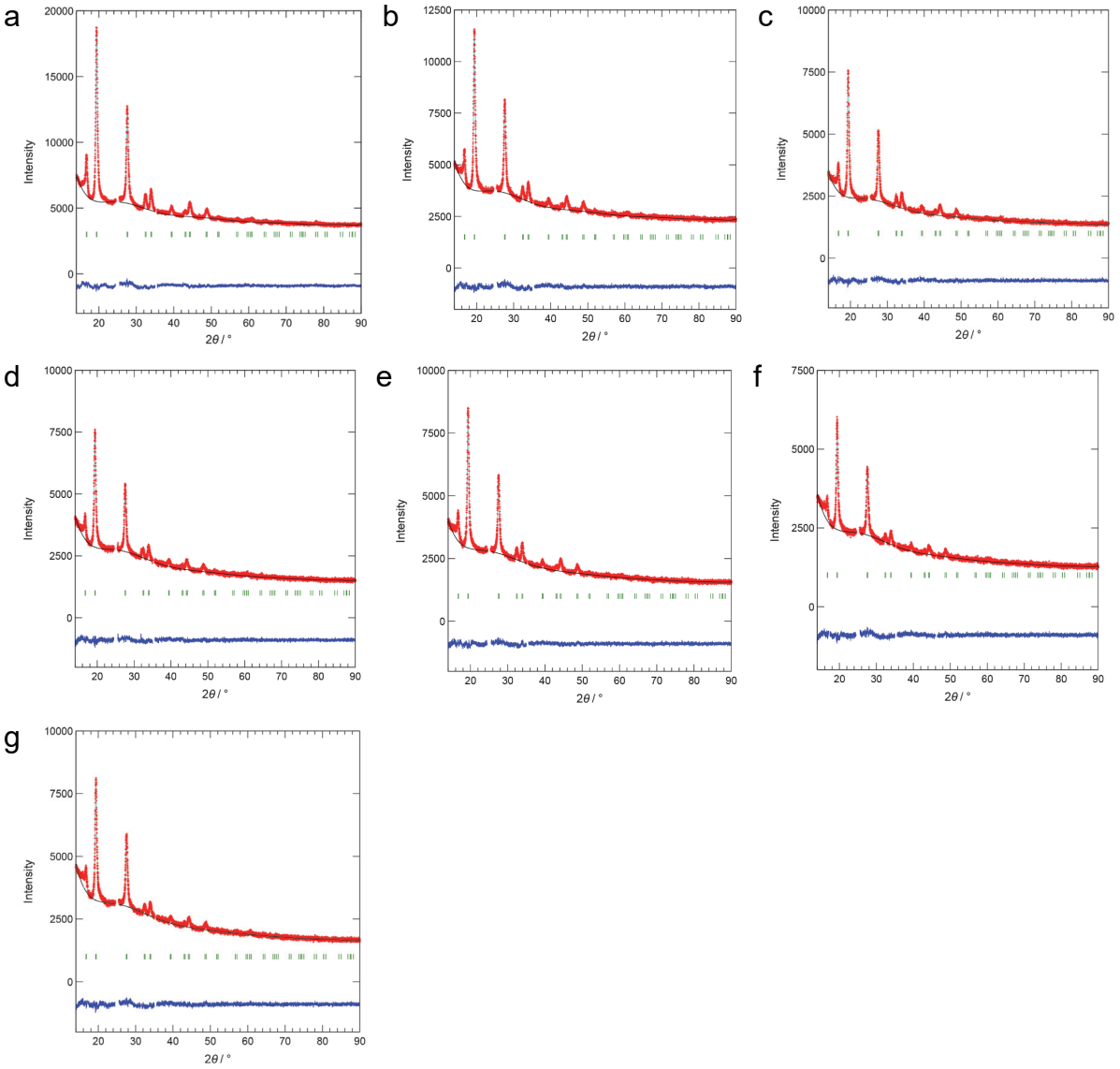

Figure S14. Fitting results of Rietveld refinement of M7O. (a) As-synthesized state. (b) 1st charged. (c) 1st discharged. (d) 2nd charged. (e) 2nd discharged. (f) 34th charged. (g) 34th discharged. Red points, cyan, black, and blue lines, and green line segments are experimental data points, best-fit curve, background curve, residual curve, and peak positions, respectively. Some 2θ regions were excluded from the fit because of the superlattice peaks and the Al current collector.

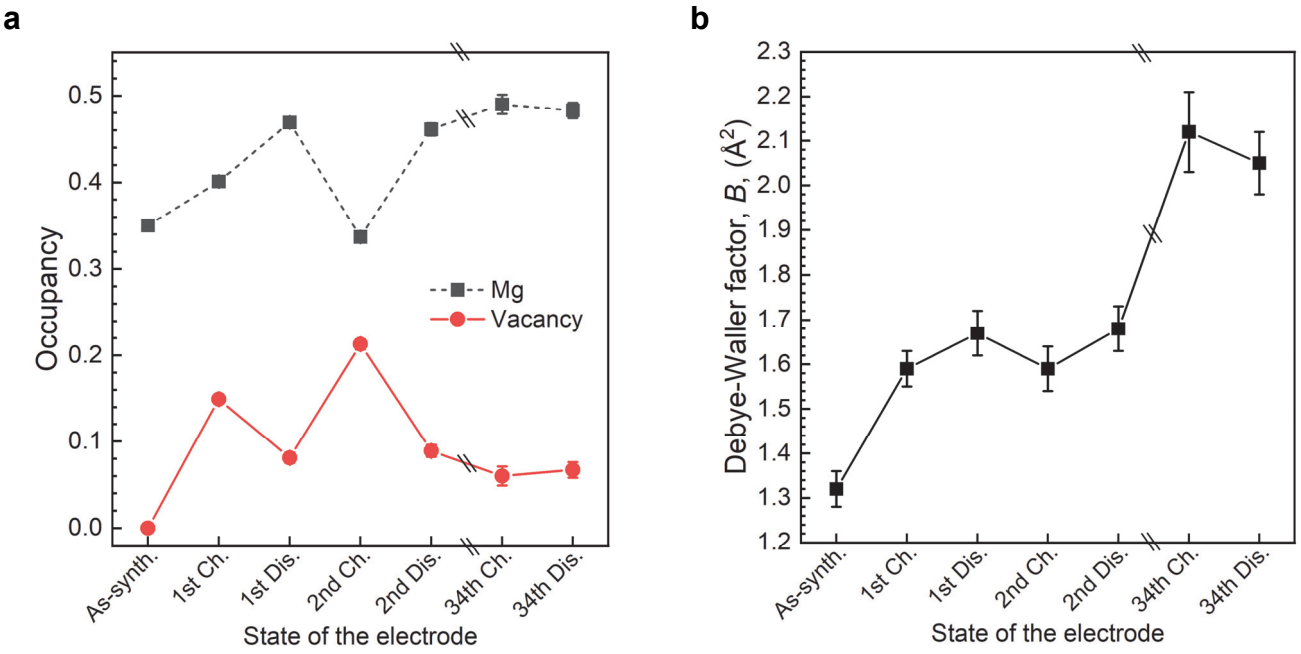

Figure S15. Structure parameters of M7O determined by the Rietveld analyses. (a) Occupancy of Mg and cation vacancy at the cation site in the disordered rocksalt structure (4a site in a space group of $Fm\bar{3}m$ (#225)). (b) Debye-Waller factor of the transition metals in M7O. Note that there were virtually no vacancies in the as-synthesized state, while cation vacancies should be formed in subsequent electrochemically charged/discharged states by extracting Li and Mg.

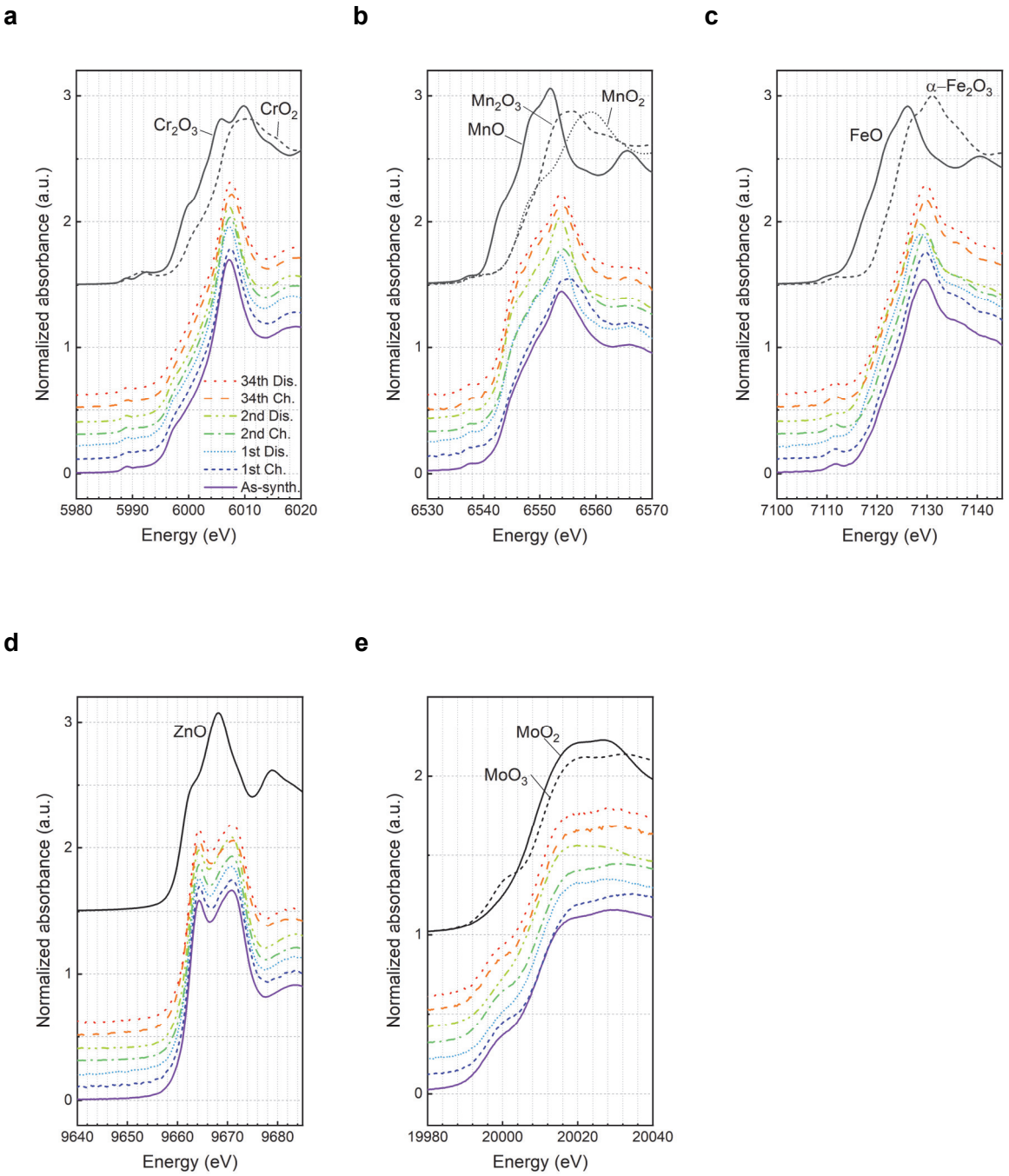

Figure S16. X-ray absorption near edge structure (XANES) at K-edges of the as-synthesized and cycled electrodes. (a) Cr, (b) Mn, (c) Fe, (d) Zn, and (e) Mo. Solid purple, short broken blue, short dotted cyan, dash-dot green, dash-dot-dot lime, broken orange, and red dot lines, i.e., lines from bottom to top at the lower part of each panel, are for the as-synthesized, 1st charged, 1st discharged, 2nd charged, 2nd discharged, 34th charged, and 34th discharged, respectively.

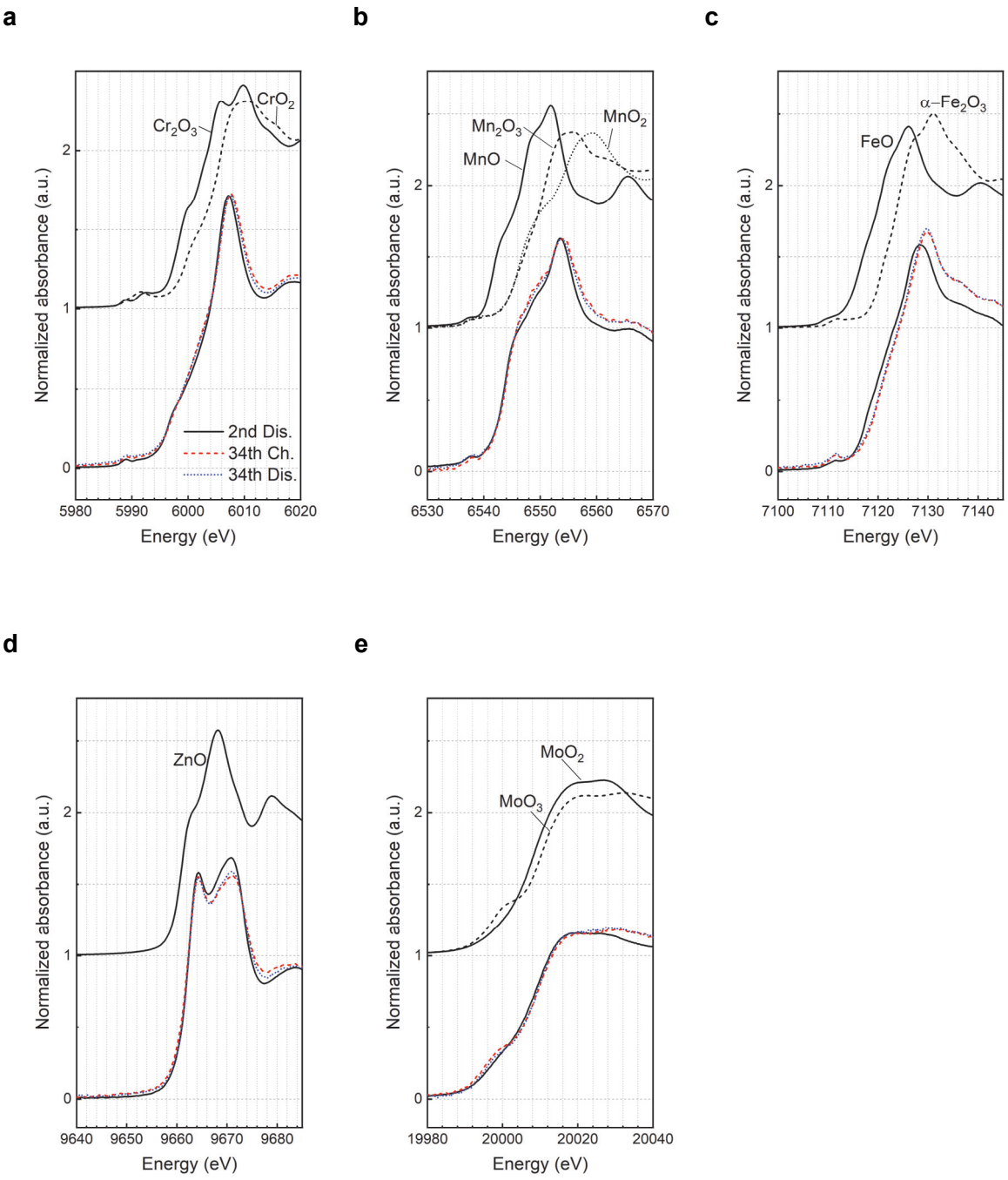

Figure S17. Comparison of XANES at the (solid black line) 2nd discharged, (broken red line) 34th charged, and (dotted blue line) 34 discharged states. (a) Cr, (b) Mn, (c) Fe, (d) Zn, and (e) Mo.

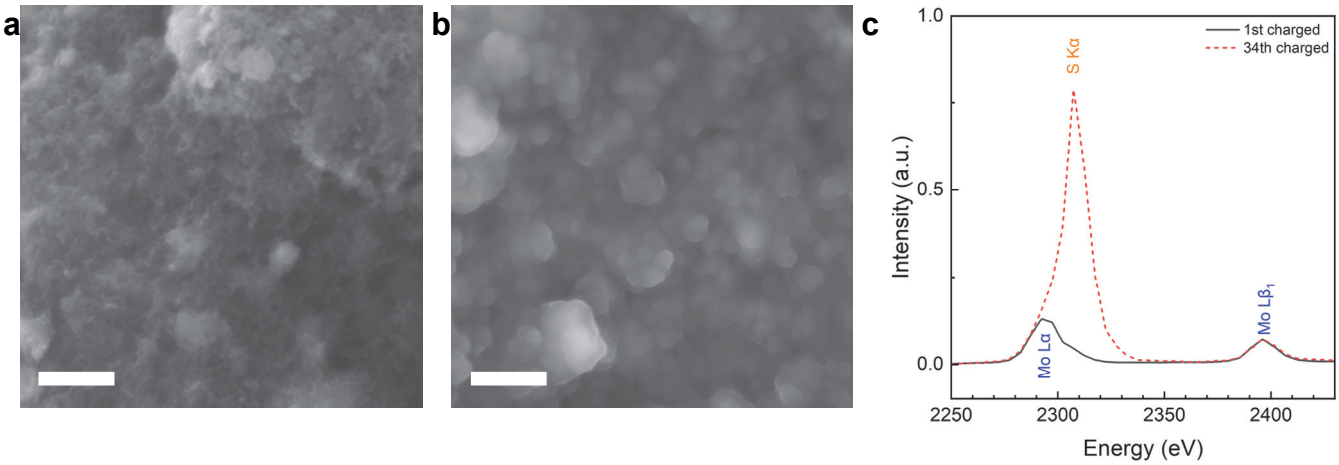

Figure S18. Scanning electron microscopy (SEM) images and X-ray fluorescence spectra from the cycled electrodes. SEM images at (a) the 1st and (b) 34th charged states. The scale bars are 2 μm. (c) X-ray fluorescence spectra of the corresponding to each electrode state.

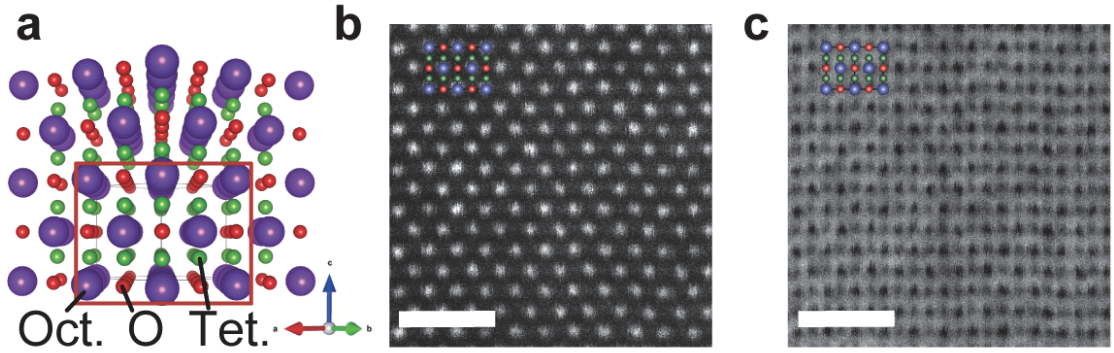

Figure S19. Scanning transmission electron microscopy (STEM) of the 2nd charged M7O. (a) Perspective view of cubic rocksalt oxide of M7O along [110] direction. Tet. and Oct. represent tetrahedral and octahedral cation sites in the FCC oxygen sublattice, respectively. (b) HAADF-STEM image along [110]. (c) ABF-STEM image along [110]. In (b) and (c), superimposed atomic illustrations show the positions of atomic columns. The scale bars in b and c are 1 nm.

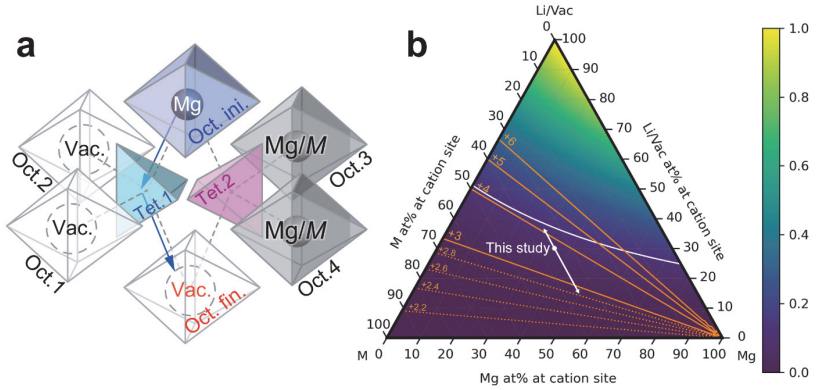

Figure S20. Two-vacancy path and percolation probability. (a) The two-vacancy path via a tetrahedral site facing two vacancies (Oct. 1 and 2) at interfering octahedral sites (Oct. 1-4) in the rocksalt structure. (b) Probability of the two-vacancy path as a function of the composition. In (a), each polyhedron is defined by oxygen atoms at their vertexes. Oct. ini. and Oct. fin. are the octahedral sites for a given hopping Mg atom and destination vacancy, respectively, where Tet. 1 and 2 are the intermediate tetrahedral sites for Mg hopping. Gray broken lines connecting two polyhedrons represent their face-sharing geometry. Solid blue arrows indicate expected hopping paths whose probabilities are visualized in (b). In (b), random vacancy distribution was assumed to calculate the percolation probability of the two-vacancy path. A white solid line is a contour curve of the critical bond-percolation probability of 0.120 for opening two-vacancy channels throughout the whole particles. Orange lines indicate the average valence state of the constituent metal elements, *M*, other than guest Mg/Li after complete delithiation. White points and arrows represent the initial composition and possible composition range determined by the expected valence change of *M* in M7O, respectively.

The present percolation probabilities of the two-vacancy path would be overestimated in light of the formation energy of the successive triple vacancies that yield the two-vacancy path (Oct.1, 2, and fin. in Figure S20a). In the two-vacancy path, Mg is stabilized at the intermediate tetrahedral site by 1007 meV from the original octahedral site in the MgO model structure (Fig. 4c). This energy landscape implies that such successive triple vacancies would be so unstable that neighboring Mg spontaneously migrates to one of the triple vacancies and/or the intermediate tetrahedral site and eventually decrease the two-vacancy paths in the material. Indeed, the occupation of the tetrahedral site by the cations including Mg, which the two-vacancy paths expectedly induce, was hardly observed by either annular bright-field (ABF)- or HAADF-STEM in the charged sample (Figure S19). This indicated that the two-vacancy paths would be minor enough to be virtually negligible for the Mg diffusion in the present DRX material.

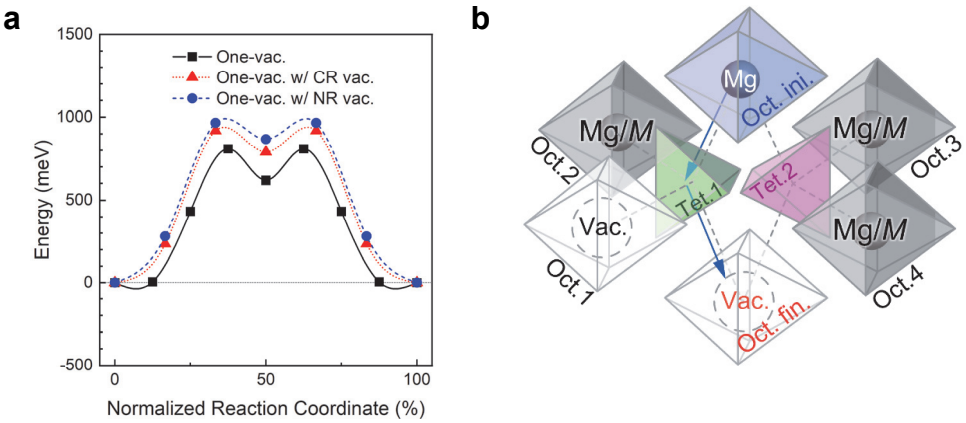

Figure S21. Energy barriers of Mg hopping in the one-vacancy path. (a) Black square, red triangle, and blue circle indicate the energy barriers of Mg hopping in the one-vacancy paths without vacancy at Oct.3-4, one vacancy at Oct. 3, and that at Oct. 4, respectively. (b) One-vacancy path and its neighboring environment.

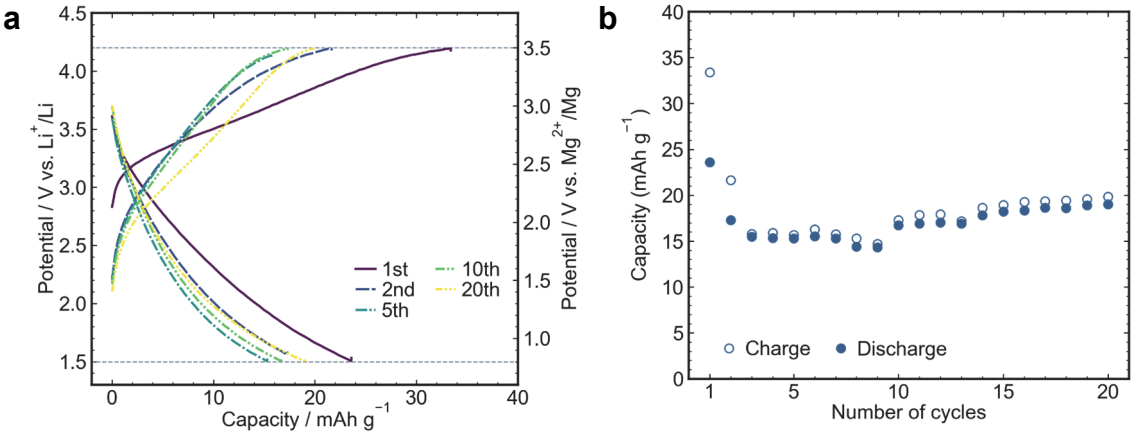

Figure S22. (a) Charge and discharge profiles of M7O at room temperature with a current density of 10.4 mA g^{-1} within the potential window of 4.2 and 1.5 V for charging and discharging, respectively. (b) Capacity retention corresponding to (b). The electrolyte of 2.26 M $Mg(TFSA)_2$ in G3 was used for the tests at room temperature.

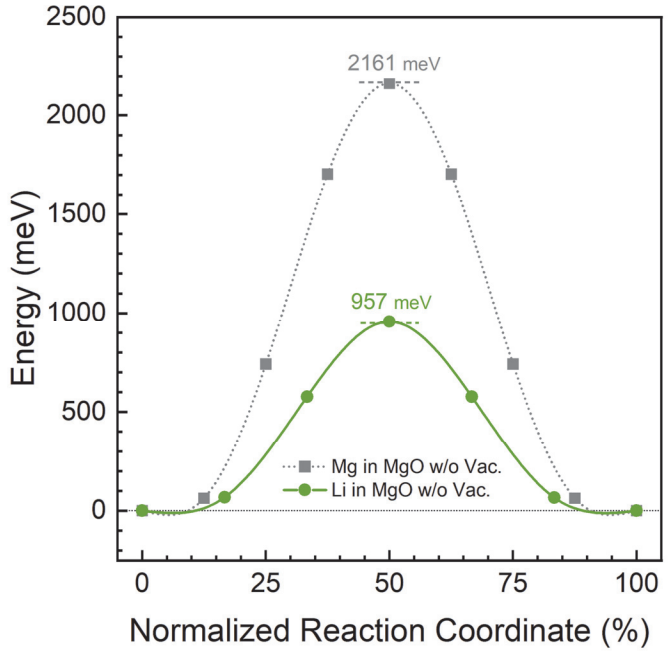

Figure S23. The energy barrier of cation hopping in MgO. Gray dotted and green solid lines indicate the minimum energy paths for Mg and Li hopping in the rocksalt MgO structure, respectively.

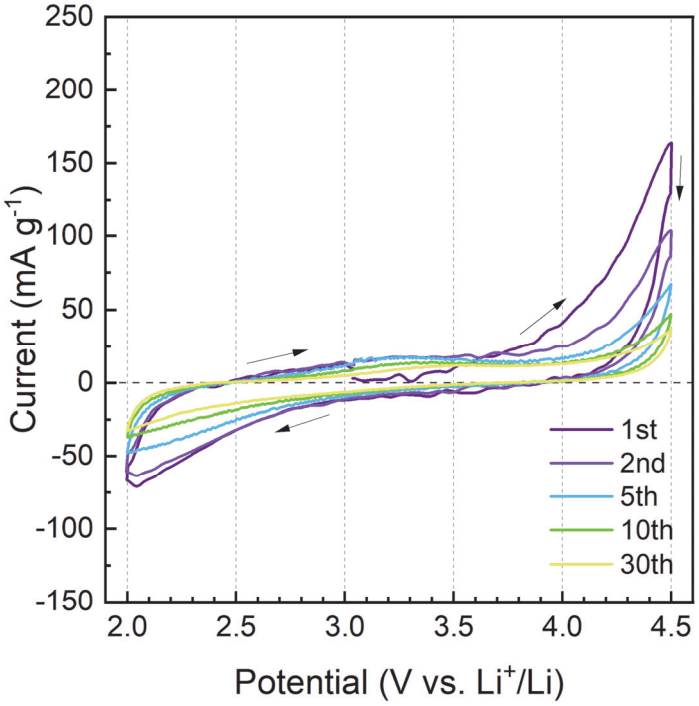

Figure S24. Cyclic voltammogram of the $Mg_{0.5}Li_{0.1}Cr_{0.1}Mn_{0.1}Fe_{0.1}Zn_{0.1}O$ between 2.0 and 4.5 V vs. Li^+/Li with a scanning speed of 1 mV s^{-1} at 90 °C.

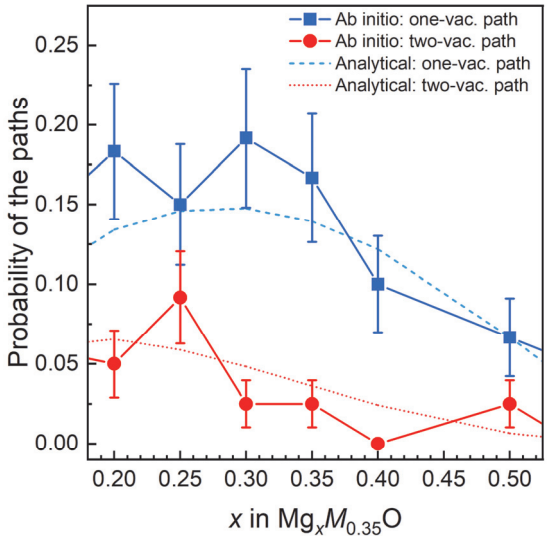

Figure S25. Probability of the one- and two-vacancy path. Blue rectangles and red circles connected by solid lines indicate the probabilities of the one- and two-vacancy path, respectively, evaluated numerically from the model structures, in which the distribution of Mg and cation vacancies were optimized to minimize the formation energy by ab initio calculation shown in Figure S1(b). Blue broken and red dotted lines indicate the probability of the one- and two-vacancy path analytically calculated on the assumption of the random distribution of Mg and vacancies, i.e., $P'_{\mathrm{one}} = 8P_{\mathrm{Mg}}P_{\mathrm{Vac}}^2(1-P_{\mathrm{Vac}})(1-P_{\mathrm{Vac}}+P_{\mathrm{Vac}}^2)$ and $P'_{\mathrm{two}} = 2P_{\mathrm{Mg}}P_{\mathrm{Vac}}^3(2-P_{\mathrm{Vac}}^2)$. Note that P'_{one} and P'_{two} were derived on the premise that there are the Mg-vacancy paths to compare the numerically determined values, which is in contrast to P_{one} and P_{two} shown in Fig. 4d Figure S20b.

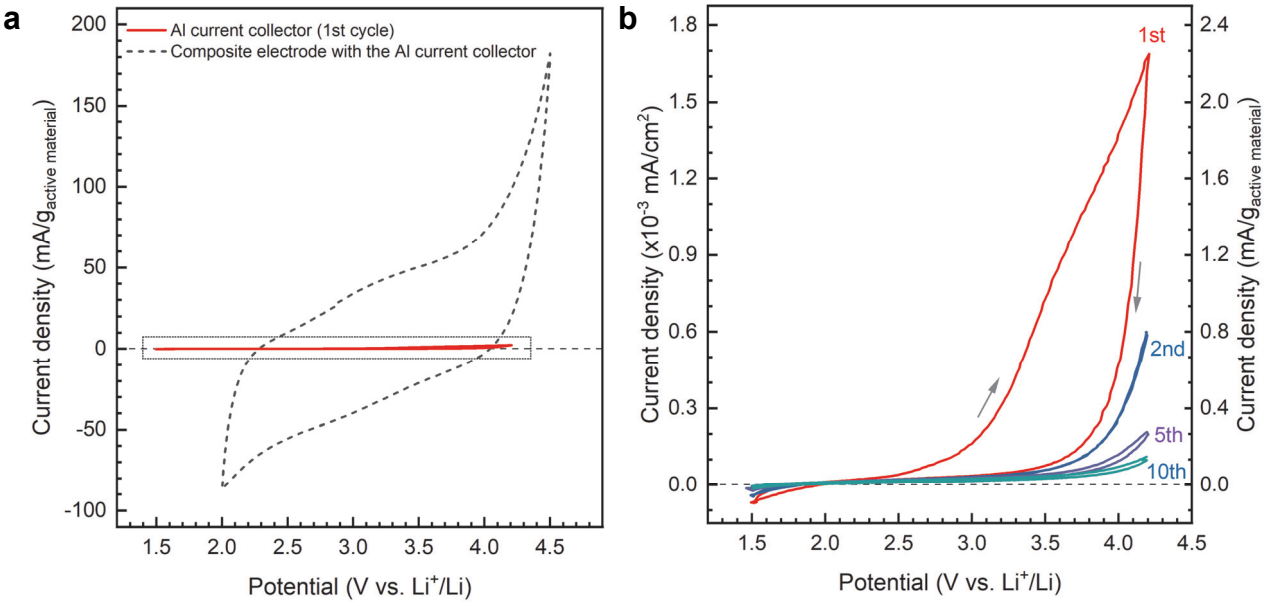

Figure S26. (a) Comparison of cyclic voltammograms of (red solid line) the bare Al current collector and (gray broken line) that with the composite electrode (2nd cycle of Fig. 2a). The current of the bare Al was normalized by the typical mass of the active material (1.5 mg) for comparison. (b) The magnified cyclic voltammogram of the bare Al indicated by the dotted-line rectangle in (a).

Table S1. Structure parameters of the as-synthesized M7O determined by the EXAFS fit. Numbers in brackets indicate the standard deviations in the last digit, e.g., 1.97(13) = 1.97 ± 0.013.

M_c	M_c-O_1		M_c-M		ΔE_0	R
	d (Å)	σ^2 ($\times 10^2$ Å^2)	d (Å)	σ^2 ($\times 10^2$ Å^2)	(eV)	(%)
Cr	1.97(13)	0.4(2)	2.92(3)	0.5(4)	−11(2)	2.7
Mn	2.09(6)	3(12)	3.0(11)	1.2(5)	−1.5(11)	0.3
Fe	2.00(3)	1.2(2)	2.99(4)	0.8(3)	−8(5)	3.6
Zn	2.05(6)	1.5(5)	2.95(7)	0.4(4)	−5(9)	8.3

Table S2. Chemical composition of the as-synthesized material determined by the inductively-coupled plasma optical emission spectroscopy (ICP-OES) analysis. The total number of cations was normalized to one to compare the target compositions.

	Mg	Li	Cr	Mn	Fe	Zn	Mo	O
Exp. (ICP-OES)	0.367	0.276	0.109	0.052	0.049	0.041	0.105	-
cf. target	0.35	0.3	0.1	0.05	0.05	0.05	0.1	1

Table S3. The chemical composition of the as-synthesized material is determined by the energy dispersive spectroscopy (EDS) analysis of the SEM image shown in Figure S6. The cation ratios were normalized by the amount of oxygen. The Li composition, denoted in the brackets, was calculated as a reference value from the other measured amount of the cations so that the total of the cation composition is one because Li was undetectable by the EDS detector in the present study.

	Mg	Li	Cr	Mn	Fe	Zn	Mo	O
Exp. (EDS)	0.367	(0.275)	0.101	0.053	0.054	0.050	0.100	1
cf. target	0.35	0.3	0.1	0.05	0.05	0.05	0.1	1

Table S4. Structure parameters of M7O determined by the Rietveld refinement. Numbers in brackets indicate the standard deviations in the last digit, e.g., 1.32(4) = 1.32 ± 0.04. The numbers without standard deviation were fixed parameters.

State	Element	Site	Occupancy	*x*	*y*	*z*	*B*
As-synth a = 4.2218(4) S = 1.2670	Mg^{2+}/Li^{+}	4a	0.65	0	0	0	1.0
	M	4a	0.35	0	0	0	1.32(4)
	O	4b	1	0.5	0.5	0.5	0.51(4)
1st Ch. a = 4.2195(15) S = 1.1477	Li^{+}	4a	0.10	0	0	0	1.8
	Mg^{2+}	4a	0.401(5)	0	0	0	0.31
	M	4a	0.35	0	0	0	1.59(4)
	O	4b	1	0.5	0.5	0.5	0.51
1st Dis. a = 4.2237(16) S = 1.0204	Li^{+}	4a	0.10	0	0	0	1.8
	Mg^{2+}	4a	0.469(6)	0	0	0	0.31
	M	4a	0.35	0	0	0	1.67(5)
	O	4b	1	0.5	0.5	0.5	0.51
2nd Ch. a = 4.2188(19) S = 1.0373	Li^{+}	4a	0.10	0	0	0	1.8
	Mg^{2+}	4a	0.337(6)	0	0	0	0.31
	M	4a	0.35	0	0	0	1.59(5)
	O	4b	1	0.5	0.5	0.5	0.51
2nd Dis. a = 4.2247(16) S = 1.0343	Li^{+}	4a	0.10	0	0	0	1.8
	Mg^{2+}	4a	0.461(7)	0	0	0	0.31
	M	4a	0.35	0	0	0	1.68(5)
	O	4b	1	0.5	0.5	0.5	0.51
34th Ch. a = 4.2253(2) S = 1.0608	Li^{+}	4a	0.10	0	0	0	1.8
	Mg^{2+}	4a	0.49(11)	0	0	0	0.31
	M	4a	0.35	0	0	0	2.12(9)
	O	4b	1	0.5	0.5	0.5	0.51
34th. Dis a = 4.2245(2) S = 1.0805	Li^{+}	4a	0.10	0	0	0	1.8
	Mg^{2+}	4a	0.483(9)	0	0	0	0.31
	M	4a	0.35	0	0	0	2.05(7)
	O	4b	1	0.5	0.5	0.5	0.51

References

1 K. Shimokawa, T. Atsumi, N. L. Okamoto, T. Kawaguchi, S. Imashuku, K. Wagatsuma, M. Nakayama, K. Kanamura and T. Ichitsubo, *Adv. Mater.*, 2021, **33**, 2007539.

2 J. Wang, J. Polleux, J. Lim and B. Dunn, *J. Phys. Chem. C*, 2007, **111**, 14925–14931.

3 L. Wang, Z. Wang, P. E. Vullum, S. M. Selbach, A. M. Svensson and F. Vullum-Bruer, *Nano Lett.*, 2018, **18**, 763–772.